ADVANCED FUNCTIONAL MATERIALS
www.afm-journal.de

Design of Metal Aerogels-Based 3D SERS Substrates by Gentle Compression

Lin Zhou, Yu Liu, Yanli Li, Chunlei Long, Shujin Zhou, René Hübner, Yueqi Li, Geng Xue, Dejun Lin, Weigao Xu, Yue Hu,* and Ran Du**

Metal aerogels (MAs) are emerging all-nanometal-structured self-standing porous materials featuring exceptional performances in diverse fields. They have recently been adopted as 3D surface-enhanced Raman scattering (SERS) substrates, while the less utilization of the unique porous structure leads to limited performance. Here, a fascinating compression-mediated regulation strategy is presented to largely boost the SERS performance of Au–Ag aerogels. By gently pressing, both the density of hot spots and the inter-ligament distance can be efficiently modulated, thus enabling to flexibly manipulate the SERS properties of MAs. On this basis, a record-high misfocus tolerance (~8.8 mm), low detection limit (down to 0.1 nM), high stability (>1 month), reusability, and multiplex detection ability are concurrently realized. This study may point out a new direction for engineering 3D SERS substrates with tunable and exceptional performance.

1. Introduction

As one of the youngest members in the aerogel family, metal aerogels (MAs) are characterized as self-standing porous materials entirely made up of nanostructured metals.[1,2] Since their discovery in 2009,[3] tremendous efforts have been made to expand the composition/structure diversity[4–9] and investigate application potential[10–13] due to their fascinating properties. In this context, the use of MAs has been expanded from electrocatalysis, sensing, programmable actuators, and to surface-enhanced Raman scattering (SERS).[6,14–18]

SERS is one of the most sensitive detection techniques that can reach the single-molecule level, which is realized by the substantially enhanced local electromagnetic field triggered by nanostructured noble metals.[19,20] Conventionally, SERS is performed on a 2D flat substrate deposited with nanostructured metals.[21–24] Due to the limited active adsorption sites and poor misfocus tolerance, 3D SERS substrates have gained increasing attention.[25] However, many reported 3D SERS substrates only have a z-axis height of a few micrometers,[26–28] which is insufficient to address the aforementioned issues. An interesting aerosol-based SERS platform with a z-axis height of up to 2.3 cm was reported recently,[29] while it is only validated for airborne analytes.

In comparison with other 3D SERS substrates, the porous millimeter- to centimeter-height (z-axis) MAs sustain extended hot spots and adsorption sites for analytes along three dimensions, thus potentially affording high Raman signal enhancement and large misfocus tolerance. Several studies reported that structure-tailored MAs display better SERS performances compared to metal NPs or flat metallic substrates.[18,30,31] Considering the nano-size effect, we systematically studied and revealed the ligament-size-dependent SERS properties of Au aerogels, offering a guideline to optimize the SERS performance.[32] However, the aforementioned studies can only modulate SERS performance by tediously adjusting the synthetic parameters, which is not desired for practice.

It is known that the intensity of the local electric field triggered by the incident light—which dictates the SERS performance—is sensitive to the distance between metallic nanostructures. On this basis, we developed here a facile compression-mediated method to flexibly tune and boost the SERS performance of Au–Ag aerogels by taking advantage of the porous and compressible

L. Zhou, Y. Liu, Y. Li, G. Xue, D. Lin, Y. Hu
Key Laboratory of Carbon Materials of Zhejiang Province
College of Chemistry and Materials Engineering
Wenzhou University
Wenzhou 325000, China
E-mail: yuehu@wzu.edu.cn
L. Zhou
School of Chemical and Material Engineering
Jiangnan University
1800 Lihu Road, Wuxi, Jiangsu Province 214122, China
C. Long, Y. Li, R. Du
School of Materials Science & Engineering
Beijing Institute of Technology
Beijing 100081, China
E-mail: rdu@bit.edu.cn
S. Zhou, W. Xu
Key Laboratory of Mesoscopic Chemistry
School of Chemistry and Chemical Engineering
Nanjing University
Nanjing 210023, China
E-mail: xuwg@nju.edu.cn
R. Hübner
Helmholtz-Zentrum Dresden-Rossendorf
Institute of Ion Beam Physics and Materials Research
Bautzner Landstrasse 400, 01328 Dresden, Germany
R. Du
Tangshan Research Institute
Beijing Institute of Technology
Tangshan 063000, China

The ORCID identification number(s) for the author(s) of this article can be found under https://doi.org/10.1002/adfm.202412006

DOI: 10.1002/adfm.202412006

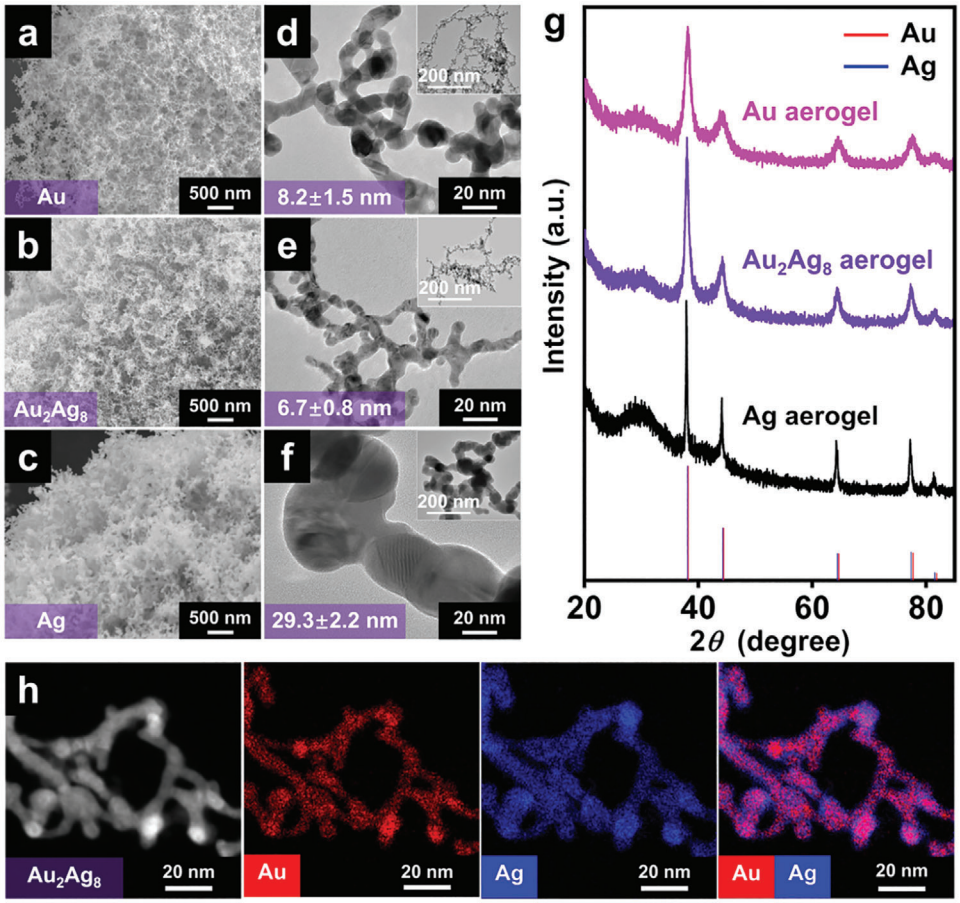

Figure 1. Structure characterizations of indicated MAs. a–c) SEM images, d–f) TEM images, and g) XRD patterns (PDF#04-0784 for Au and PDF#04-0783 for Ag). h) High-angle annular dark-field scanning transmission electron microscopy (HAADF-STEM) images and corresponding energy-dispersive x-ray spectroscopy (EDX) mappings.

features of aerogels. The pore size of MAs can be easily adjusted by gently pressing. This enables the modulation of the density of "hot spots" and inter-ligament distance, thus realizing the control of SERS properties. By using the appropriately compressed Au_8Ag_2 aerogel as the SERS substrate, we cannot only implement the focus step with a low-magnification 5× objective lens, but also concurrently realize a record-high misfocus tolerance (>8.8 mm), low detection limit (0.1 nM), high stability (>1 month), reusability, and multiplex detection ability. Therefore, this study may open a new door for designing aerogel-based 3D substrates with excellent and highly tunable SERS performance.

2. Results and Discussion

2.1. Fabrication and Characterizations of Metal Aerogels

Single-component Au and Ag aerogels, as well as bi-metallic Au–Ag and Au–Pd aerogels were fabricated based on our previously developed salt-induced methods[6] (see Experimental Section). Au–Ag aerogels with various Au/Ag ratios were prepared and denoted as Au_xAg_y, where x/y indicates the molar ratio of Au to Ag involved in the precursors.

To investigate the composition effect on the morphology and ligament size, scanning electron microscopy (SEM) and transmission electron microscopy (TEM) were performed. According to **Figures** 1a–f and S1 and S2 (Supporting Information), all aerogels feature highly porous networks. Except for a relatively large ligament size for the Ag aerogel (29.3 ± 2.2 nm), the ligament sizes of all other Au–Ag samples are close to each other (6.3–8.2 nm, see Figure S3, Supporting Information) and they feature specific surface areas of 15.4–27.9 $m^2\ g^{-1}$ (Figure S4 and Table S1, Supporting Information). The crystalline structure was determined by X-ray diffraction (XRD) (Figure 1g; Figures S5 and S6, Supporting Information), where the presence of sharp diffraction peaks suggests good crystallinity of all as-obtained aerogels (the weak hump located at ~30° comes from the sample holder). The difference in the peak width could be associated with the difference in both the crystalline size and chemical composition of those aerogels.[8]

To evaluate the composition of the obtained Au–Ag aerogels, energy-dispersive X-ray spectroscopy (EDX) was performed (Figure S7, Supporting Information). The Au-to-Ag ratios in the initial reaction systems are in line with those in the aerogels, which allows for direct adoption of the Au-to-Ag ratios of the precursors in the following studies. Note that the spatial

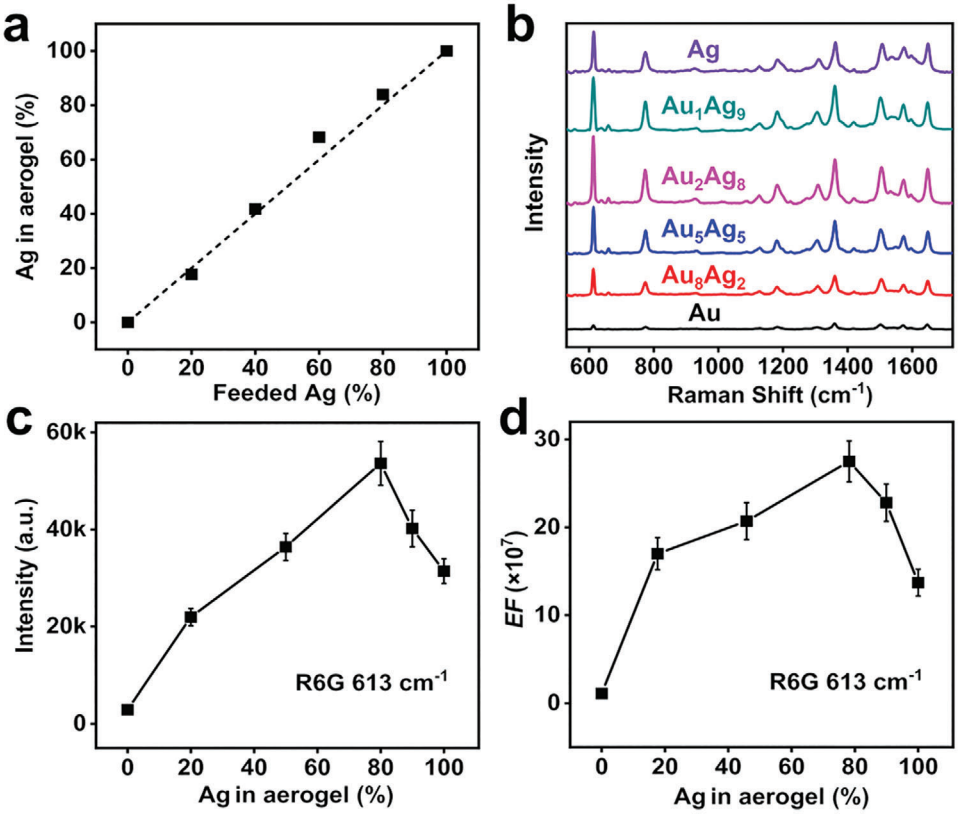

Figure 2. Composition-dependent SERS properties of aerogels. a) Ag proportion in the aerogels versus that in the precursors (i.e., feeded Ag). b) Raman spectra of R6G on aerogels with different Ag proportion using an excitation wavelength of 532 nm. Plots of the c) Raman intensity and the d) *EF* versus the Ag proportion in the aerogels.

element distribution is also critical for bimetallic aerogels. Scanning transmission electron microscopy imaging combined with STEM-EDX discloses a composition-dependent element distribution (Figure 1h; Figures S8 and S9, Supporting Information). An Au–Ag core–shell structure was found for aerogels with ≥20% gold (i.e., Au_2Ag_8, Au_5Ag_5, and Au_8Ag_2 aerogels), as observed previously,[6,8] which is attributed to the segregation of the low-surface-energy metal on the high-surface-energy one.[33] The exposed highly SERS-active Ag shell may promote the detection performance compared to Au or Au–Ag alloy. Interestingly, certain Ag–Au core–shell structures were found for the Au_1Ag_9 aerogel. This may result from a faster formation of Ag nanostructures as nuclei due to the much higher concentration of Ag^+ compared to that for $AuCl_4^-$, on which the Au shell will deposit via either reduction by $NaBH_4$ or by Galvanic replacement reaction.

2.2. Composition-Dependent SERS Properties

The aerogels structured from Au, Ag, and Au–Ag have been reported for SERS applications, while a systematic investigation of the composition-dependent SERS properties is lacking. Here, the Au, Au_8Ag_2, Au_5Ag_5, Au_2Ag_8, Au_1Ag_9, and Ag aerogels were adopted to clarify the composition effect by using rhodamine 6G (R6G) as a probe, and the loading period for the probe is optimized to be ~24 h.

As seen in **Figures** 2a–c and S10 (Supporting Information), the Raman intensity stepwise grows stronger with increasing Ag proportion ranging from 0% to 80%, while it becomes weaker for the bare Ag. The enhanced performance with a higher Ag proportion could be attributed to the intrinsically high SERS activity of Ag compared to that of Au. Particularly, the as-mentioned Au–Ag core–shell structure can largely expose the highly SERS-active Ag component, thus boosting the performance. Further increase of the Ag content, however, leads to a substantial increase of the ligament size to 29.3 nm for the Ag aerogel. This reduces the available adsorption sites for analytes and thus deteriorates the SERS performance. From Figure 2d and Table S2 (Supporting Information), the calculated enhancement factors (*EFs*) for the aforementioned Au–Ag aerogels follow a similar trend, which achieves the maximized value of 2.75×10^8 at 613 cm^{-1} for the Au_2Ag_8 aerogel. This value considerably outperforms the single-component Au and Ag aerogels (1.09×10^7 and 1.37×10^8, respectively), highlighting the importance of composition modulation for performance optimization. Therefore, the optimized Au_2Ag_8 aerogel was selected for the following studies.

2.3. Compression-Modulated SERS Properties

Au–Ag aerogels feature a 3D porous structure that allows light penetration. Hence, most probe molecules within the 3D

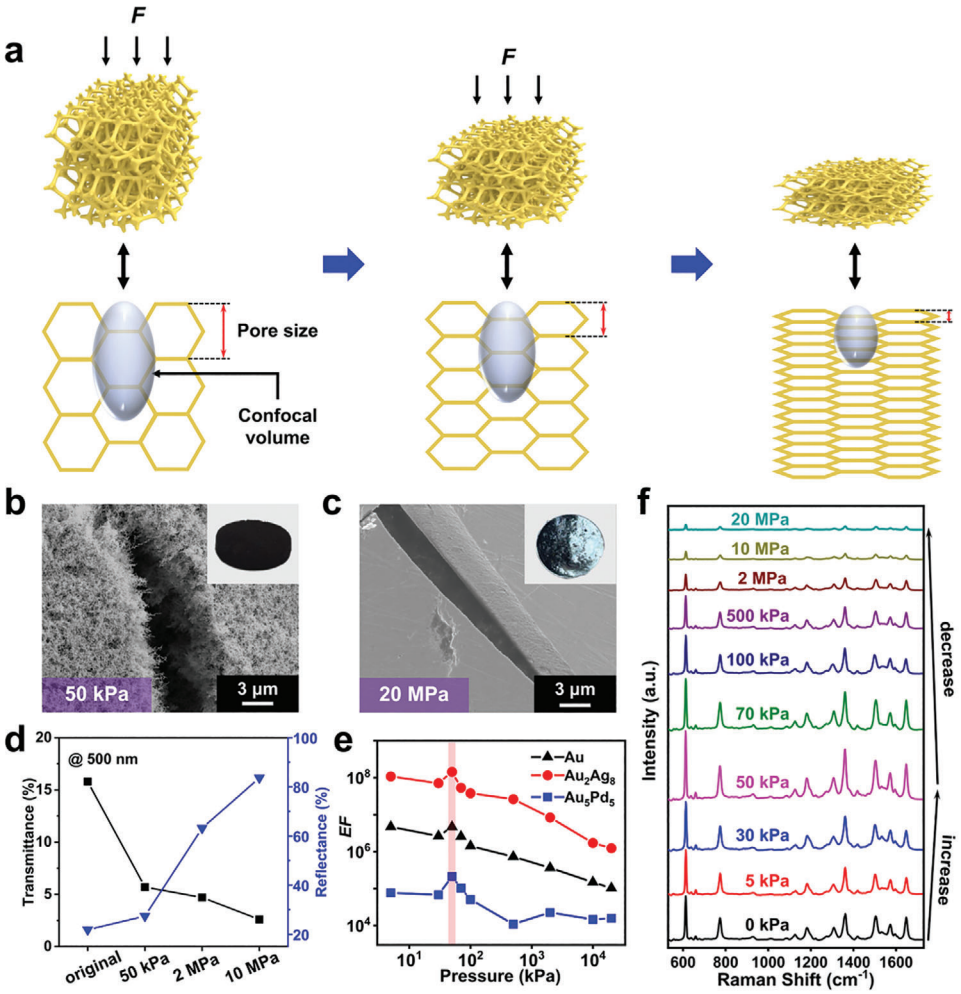

Figure 3. Compression-modulated SERS properties of metal aerogel. a) Schematic structure evolution of the aerogel upon compression. b,c) SEM images and digital photos of the Au_2Ag_8 aerogel compressed at 50 kPa and 20 MPa, respectively. d) The transmittance and reflectance recorded at 500 nm for the Au_2Ag_8 aerogel compressed at different pressures. e) Relative density and *EF* of the indicated aerogels versus the applied pressure. f) Raman spectra of the Au_2Ag_8 aerogel for various applied pressures. The probe is R6G and the calculation in (e) was based on the peak centered at 613 cm^{-1}.

confocal volume will be excited and detected upon irradiation for aerogel-based 3D SERS substrates. In this regard, the detected Raman signal should positively correlate to the number of hot spots within the confocal volume. Hence, to further boost the SERS performance, one feasible way is to increase the density of the aerogel and thus the density of hot spots. However, the manipulation of the density of hot spots in MAs has not been achieved yet.

Our previous study shows that MAs are highly compressible, where a more than 98% volume reduction can be reached by manually pressing.[6] As schemed in **Figure** 3a, on the one hand, the pore size of the aerogel will decrease upon compression, resulting in a larger density. Because light can hardly penetrate metal, the density increase will result in an overall decreased refractive index, thus reducing the size of the confocal volume. On the other hand, the density of hot spots will increase with decreasing pore size. Additionally, the *z*-direction gap between metal ligaments is also reduced along with compression, which can enhance the strength of the inter-nanowire electromagnetic field and thus contribute to enhanced signal enhancement. Therefore, the interplay between the reduced confocal volume, the increased density of hot spots, and the decreased gap between metal ligaments will co-govern the SERS performance of MAs.

Based on the above analysis, the Au_2Ag_8 aerogel was compressed at different pressures from 0 to 20 MPa. The corresponding sample is denoted as Au_2Ag_8-*p*, where *p* indicates the adopted pressure. The structure change is identified by SEM (Figure 3b–c and Figure S11, Supporting Information), which reveals that pressuring flattens the surface, reduces the porosity, and densifies the structure of the aerogel. The porosity and pore size reduction is also evidenced by the nitrogen adsorption tests with the pressure rising from 0 to 20 MPa (Figure S12 and Table S3, Supporting Information). Such compression-led structure evolution was also observed for the Au and Au_5Pd_5 aerogels (Figures S14 and S15, Supporting Information). Along with the pore volume reduction, the density of all aerogels increases accordingly (Figure S15, Supporting Information),

eventually reaching values 20–30 times higher than those for the uncompressed ones.

Apart from the structure change, we have also characterized the optical properties of uncompressed and compressed Au_2Ag_8 aerogel. As displayed in Figure 3d and Figure S16 (Supporting Information), the light transmission decreases while the reflectance increases along with pressuring. This can be rationalized by the very small skin depth and large real refractive index of electrically conductive metals. Once a densified networked structure is formed by compression, light will interact more strongly with metal ligaments, thus causing retarded transmission and significant reflection. Therefore, excessive compression (e.g., 10 MPa) will discourage the SERS performance because the incident light is hard to excite probes located inside the compressed aerogel.

To verify the aforementioned hypothesis, Raman spectra were recorded on various compressed Au_2Ag_8 aerogels by using R6G as probes. As shown in Figure 3e,f and Figure S17 (Supporting Information), the Raman intensity increases by raising the pressure from 0 to 50 kPa, then decreases with larger pressures (50 kPa–20 MPa). The change of the *EF* shows a generally similar trend as that of the Raman intensity (Table S4, Supporting Information), achieving the maximum value at 50 kPa pressure (Au_2Ag_8-50 kPa, 1.44×10^8 at 613 cm^{-1}) within the range of 5 kPa–20 MPa. Notably, compression can also significantly increase the uniformity of measurements, with the relative standard deviation of SERS tests from 19.6% for the Au_2Ag_8 aerogel to 4.1% for the Au_2Ag_8-20 MPa aerogel (Figure S18, Supporting Information). Such compression-modulated SERS properties are attributed to concomitant effects of 1) the density of hot spots, 2) the available adsorption sites, 3) the light penetration ability, and 4) the uniformity of pore size.

With enhanced densification at the initial stage, the number density of nanostructures increases, thus increasing the density of hot spots and leading to improved Raman intensity for pressures increasing from 0 to 50 kPa. Meanwhile, the compression-induced densification will reduce the porosity of the aerogels, which discourages the penetration of the incident light for analyte excitation and the collection of the scattered light for detection, thus decreasing the received Raman signal. An intensive compression will eventually convert the 3D aerogel to an almost 2D object with limited sites for accommodating analytes. Combining the aforementioned effects, the Au_2Ag_8-50 kPa aerogel displays the largest total detected Raman signal (i.e., the Raman intensity), while its average Raman signal from each probe molecule (i.e., the calculated *EF*) is slightly lower than that for the uncompressed Au_2Ag_8 aerogel. To confirm the generality of the above analysis, studies on compression-modulated Au aerogels and Au_5Pd_5 aerogels were implemented. As displayed in Figures S18 and S19 and Tables S5 and S6 (Supporting Information), the optimized Raman intensity was also acquired at a compression of 50 kPa, which agrees with the previous results for the Au_2Ag_8 system. Therefore, the compression-modulated method may open a new perspective on facilely manipulating the SERS performance of MAs.

It is worth mentioning that both the Raman intensities and *EFs* of the Au_2Ag_8-50 kPa aerogel are more than one order of magnitude larger than those values of the optimized Au-50 kPa aerogel for a library of probes (R6G, Nile blue A (NBA), methylene blue (MB), and 4-mercaptobenzonitrile (4-MBN), see Figures S18–S20, Supporting Information), pointing out the importance of composition engineering. Moreover, the obtained *EF* for the Au_2Ag_8-50 kPa aerogel using R6G as an analyte probe (1.44×10^8) is substantially higher than that of previously reported 3D SERS substrates based on MAs or other systems (typically around 10^6).[18,26,27,29,30,32] These facts imply that both the composition and the microstructure are critical for designing high-performance MAs for SERS applications. The composition design is mainly based on the smart selection of intrinsically highly SERS-active metals, while the microstructure design focuses on modulating the density of hot spots. The aforementioned design concept not only leads to the high-performance Au_2Ag_8-50 kPa aerogel, but also points out an unambiguous way of on-target designing 3D SERS substrates for ultrasensitive detection.

2.4. Compressed Au–Ag Aerogels for SERS Detection

To fully reveal the SERS performance of the composition and density-optimized Au_2Ag_8-50 kPa aerogel, firstly, the detection limit was probed at first by using the R6G as an analyte. Usually, Raman measurement was conducted by using a relatively high-magnification objective lens (e.g., 50× objective lens) for exactly focusing the laser on the surface of the substrate. As seen from **Figure** 4a, clear Raman signals are identified at a concentration of as low as 0.1 nM (50× objective lens), outperforming previously reported Ag nanofoams (10^{-7} M) and Au–Ag aerogels (10^{-9} M).[17,29] Impressively, attributed to the 3D structure of the Au_2Ag_8-50 kPa aerogel, the same low detection limit (0.1 nM) can be acquired even by using a low-magnification 5× objective lens (Figure 4b), suggesting the vast potential of the MAs-based SERS substrate for practical use.

Second, the misfocus tolerance of the aerogel, which is the critical advantage of a 3D SERS platform compared to a conventional 2D SERS platform, was evaluated. Generally, the Au_2Ag_8-50 kPa aerogel outperforms an 8-nm-thick Au film (the benchmark 2D SERS substrate) and the Au-50 kPa aerogel at defocus values ranging from 0 to 312 μm (Figure S20, Supporting Information). As illustrated in Figure 4c, the Raman signal measured on an 8-nm-thick Au film can only be identified with a defocus of less than 100 μm. In comparison, the Au_2Ag_8-50 kPa aerogel manifests a defocus tolerance of up to 8.8 mm by using a 5× objective lens (Figure 4d). The remarkable performance of the aerogel substrate is attributed to two aspects. On the one hand, the porous aerogel allows the laser to excite the molecules below the upper surface, thus enabling the collection of Raman signals deviating from the on-focus state. On the other hand, compared to the 8-nm-thick Au film which suffers from a strong fluorescence background, the aerogel substrate substantially suppressed the fluorescence and thus acquired sharp Raman signals, which further strengthened the defocus tolerance.

Third, in the field of analytic chemistry, multiplex SERS detection is one of the most important directions for processing complicated systems. Here, combining the high sensitivity and defocus-tolerant capacity of the Au_2Ag_8-50 kPa aerogel, aqueous solutions of the mixture of common dyes (NBA, MB, and 4-MBN) were measured. For identification, the Raman shifts located at 595, 1617, and 1585 cm^{-1} are used to mark NBA, MB, and

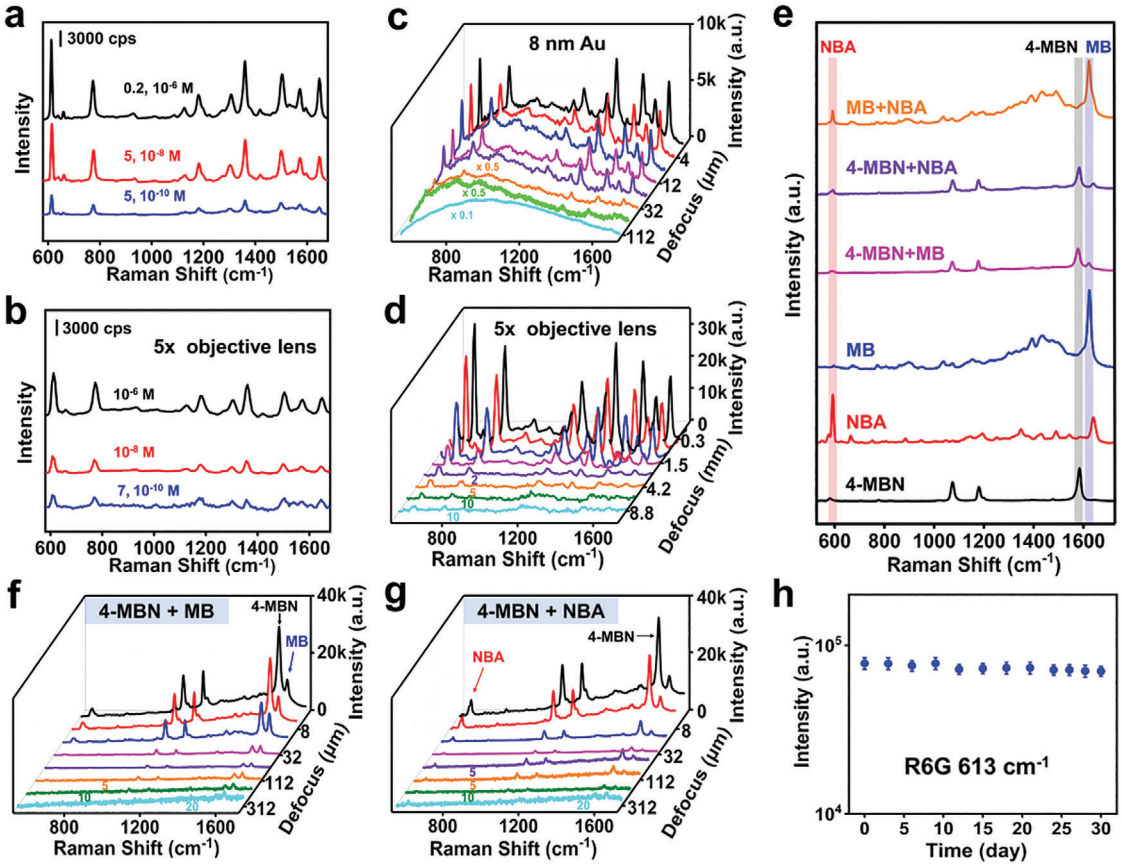

Figure 4. Comprehensive investigation of the SERS performance of the Au_2Ag_8-50 kPa aerogel. a,b) Raman spectra recorded for the Au_2Ag_8-50 kPa aerogel by testing R6G of different concentrations and different objective lenses. Cascade Raman spectra of R6G loaded on c) an 8-nm-thick Au film (50× objective lens) and d) the Au_2Ag_8-50 kPa aerogel (5× objective lens) for the indicated defocus range. e) Raman spectra recorded on the Au_2Ag_8-50 kPa aerogel loaded with one or more probe molecules. Multiplex detection of f) 10^{-4} M 4-MBN + 10^{-5} MB and g) 10^{-4} M 4-MBN + 10^{-6} M NBA on the Au_2Ag_8-50 kPa aerogel for the indicated defocus range. h) Stability test of the Au_2Ag_8-50-kPa-based SERS substrate loaded with R6G.

4-MBN, respectively. As shown in Figure 4e, the mixture of two dyes can be clearly identified on the Au_2Ag_8-50 kPa aerogel, suggesting the multi-channel detection capability. In a further step, the multiplex detection at different defocus values was conducted (Figure 4f,g). Impressively, at a misfocus of ~300 μm, different dyes can still be identified, which demonstrates the unique advantage of applying the Au_2Ag_8-50 kPa aerogel for rapid detection of multiple analytes without the need for a tight focus.

Finally, the long-term stability and reusability of the Au_2Ag_8-50 kPa aerogel were tested to evaluate their practical value. The Raman intensity for R6G remains almost the same after one month of exposure to air (Figure 4h), suggesting the high stability of the aerogel substrate. Additionally, our aerogels can be repeatedly used, which sustain preserved performance for 10 cycles (Figure S25, Supporting Information). Overall, the Au_2Ag_8-50-kPa-based 3D SERS substrate not only strengthens the Raman signal by accommodating more hot spots as well as analytes, but also offers excellent defocus tolerance even for multiplex detection. Moreover, the compression-modulated design smartly utilizes the monolithic and porous features of aerogels, pointing out a new way to fully take advantage of the structural features and further boost the performance of aerogels-based SERS substrates.

3. Summary

To sum up, a general and fascinating compression-mediated regulation strategy was proposed, which is capable of efficiently manipulating the density of hot spots and the inter-ligament distance of metal aerogels by gently pressing. Combining with composition investigations, a moderately compressed Au_2Ag_8-50 kPa aerogel, which displays an Au–Ag core–shell NWs-fused network, was created and displayed the best SERS performance with an *EF* of 1.44×10^8. Meanwhile, the 3D self-supported aerogel offers a record-large misfocus tolerance of ~8.8 mm, along with high stability (>1 month), reusability, low detection limit (0.1 nM achieved by using a low-magnification 5× objective lens), and multiplex detection ability, highlighting the large practical potential of applying compressible aerogels for SERS detection. The current research not only provides new insights for on-target manipulating SERS properties of aerogel-based 3D SERS platforms by simple pressing, but also promotes practical SERS detection without the need for a tight focus and high-magnification objective lens. Therefore, this study may open a new door for designing aerogel-based 3D substrates with excellent and highly tunable SERS performance.

Supporting Information

Supporting Information is available from the Wiley Online Library or from the author.

Acknowledgements

L.Z., Y.L., Y.L. and C.L. contributed equally to this work. This work was supported by the Beijing Natural Science Foundation (2232063), the National Natural Science Foundation of China (22202009, 51972237), the Natural Science Foundation of Zhejiang Province (LY19E020008), the Hebei Natural Science Foundation (B2024105005), the Basic Science and Technology Research Project of Wenzhou (G2023010), and the Experimental Center of Advanced Materials in the Beijing Institute of Technology. The use of the HZDR Ion Beam Center TEM facilities and the funding of TEM Talos by the German Federal Ministry of Education and Research (BMBF; Grant No. 03SF0451) in the framework of HEMCP are acknowledged. Furthermore, the use of the X-ray diffractometers at the Analysis & Testing Center of the Beijing Institute of Technology is acknowledged.

Conflict of Interest

The authors declare no conflict of interest.

Data Availability Statement

The data that support the findings of this study are available from the corresponding author upon reasonable request.

Keywords

3D SERS substrates, compression-mediated, metal aerogels, SERS

Received: July 8, 2024
Revised: August 12, 2024
Published online: August 22, 2024

[1] X. Jiang, R. Du, R. Hübner, Y. Hu, A. Eychmüller, *Matter* **2021**, *4*, 54.
[2] N. Wang, Y. Li, Q. Cui, X. Sun, Y. Hu, Y. Luo, R. Du, *Acta Phys.-Chim. Sin.* **2023**, *39*, 2212014.
[3] N. C. Bigall, A. K. Herrmann, M. Vogel, M. Rose, P. Simon, W. Carrillo-Cabrera, D. Dorfs, S. Kaskel, N. Gaponik, A. Eychmüller, *Angew. Chem., Int. Ed.* **2009**, *48*, 9731.
[4] A.-K. Herrmann, P. Formanek, L. Borchardt, M. Klose, L. Giebeler, J. r. Eckert, S. Kaskel, N. Gaponik, A. Eychmüller, *Chem. Mater.* **2013**, *26*, 1074.
[5] D. Wen, W. Liu, D. Haubold, C. Zhu, M. Oschatz, M. Holzschuh, A. Wolf, F. Simon, S. Kaskel, A. Eychmüller, *ACS Nano* **2016**, *10*, 2559.
[6] R. Du, Y. Hu, R. Hübner, J.-O. Joswig, X. Fan, A. Eychmüller, *Sci. Adv.* **2019**, *5*, 4590.
[7] G. Xue, Y. Li, R. Du, J. Wang, R. Hübner, M. Gao, Y. Hu, *Small* **2023**, *19*, 2301288.
[8] R. Du, J. Wang, Y. Wang, R. Hübner, X. Fan, I. Senkovska, Y. Hu, S. Kaskel, A. Eychmüller, *Nat. Commun.* **2020**, *11*, 1590.
[9] Z. Zhang, B. Zhou, M. Jia, C. Wu, T. Niu, C. Feng, H. Wang, Y. Liu, J. Lu, Z. Zhang, J. Shen, A. Du, *Sci. Adv.* **2023**, *9*, 9108.
[10] W. Li, B. Weng, X. Sun, B. Cai, R. Hübner, Y. Luo, R. Du, *Catalysts* **2023**, *13*, 167.
[11] W. Gao, D. Wen, *VIEW* **2021**, *2*, 20200124.
[12] H. Guo, D. Si, H. Zhu, Q. Li, Y. Huang, R. Cao, *eScience* **2022**, *2*, 295.
[13] Y. Li, B. Weng, J. Zhao, R. Du, *Acta Chim. Sin.* **2024**, *82*, 805.
[14] B. Cai, R. Hübner, K. Sasaki, Y. Zhang, D. Su, C. Ziegler, M. B. Vukmirovic, B. Rellinghaus, R. R. Adzic, A. Eychmüller, *Angew. Chem., Int. Ed.* **2018**, *57*, 2963.
[15] R. Du, W. Jin, R. Hübner, L. Zhou, Y. Hu, A. Eychmüller, *Adv. Energy Mater.* **2020**, *10*, 1903857.
[16] B. Jiang, Z. Wan, Y. Kang, Y. Guo, J. Henzie, J. Na, H. Li, S. Wang, Y. Bando, Y. Sakka, Y. Yamauchi, *Nano Energy* **2021**, *81*, 105644.
[17] G. Li, J. Hao, W. Li, F. Ma, T. Ma, W. Gao, Y. Yu, D. Wen, *Anal. Chem.* **2021**, *93*, 14068.
[18] X. Gao, R. J. A. Esteves, L. Nahar, J. Nowaczyk, I. U. Arachchige, *ACS Appl. Mater. Interfaces* **2016**, *8*, 13076.
[19] J. Kneipp, H. Kneipp, K. Kneipp, *Chem. Soc. Rev.* **2008**, *37*, 1052.
[20] X. Meng, L. Qiu, G. Xi, X. Wang, L. Guo, *SmartMat* **2021**, *2*, 466.
[21] M. Shao, C. Ji, J. Tan, B. Du, X. Zhao, J. Yu, B. Man, K. Xu, C. Zhang, Z. Li, *Opto-Electron. Adv.* **2023**, *6*, 230094.
[22] Z. Pei, J. Li, C. Ji, J. Tan, Z. Shao, X. Zhao, Z. Li, B. Man, J. Yu, C. Zhang, *J. Phys. Chem. Lett.* **2023**, *14*, 5932.
[23] J. Tan, B. Du, C. Ji, M. Shao, X. Zhao, J. Yu, S. Xu, B. Man, C. Zhang, Z. Li, *ACS Photonics* **2023**, *10*, 2216.
[24] C. Zhang, J. Tan, B. Du, C. Ji, Z. Pei, M. Shao, S. Jiang, X. Zhao, J. Yu, B. Man, Z. Li, K. Xu, *ACS Appl. Mater. Interfaces* **2024**, *16*, 12085.
[25] G. C. Phan-Quang, X. Han, C. S. L. Koh, H. Y. F. Sim, C. L. Lay, S. X. Leong, Y. H. Lee, N. Pazos-Perez, R. A. Alvarez-Puebla, X. Y. Ling, *Acc. Chem. Res.* **2019**, *52*, 1844.
[26] H. Liu, Z. Yang, L. Meng, Y. Sun, J. Wang, L. Yang, J. Liu, Z. Tian, *J. Am. Chem. Soc.* **2014**, *136*, 5332.
[27] R. A. Alvarez-Puebla, A. Agarwal, P. Manna, B. P. Khanal, P. Aldeanueva-Potel, E. Carbó-Argibay, N. Pazos-Pérez, L. Vigderman, E. R. Zubarev, N. A. Kotov, L. M. Liz-Marzán, *Proc. Natl. Acad. Sci. USA* **2011**, *108*, 8157.
[28] Q. Zhang, Y. H. Lee, I. Y. Phang, C. K. Lee, X. Y. Ling, *Small* **2014**, *10*, 2703.
[29] G. C. Phan-Quang, H. K. Lee, H. W. Teng, C. S. L. Koh, B. Q. Yim, E. K. M. Tan, W. L. Tok, I. Y. Phang, X. Y. Ling, *Angew. Chem., Int. Ed.* **2018**, *57*, 5792.
[30] S. Tang, S. Vongehr, Y. Wang, J. Cui, X. Wang, X. Meng, *J. Mater. Chem. A* **2014**, *2*, 3648.
[31] Y. Xiao, C. Wang, K. Liu, L. Wei, Z. Luo, M. Zeng, Y. Yi, *J. Sol-Gel Sci. Technol.* **2021**, *99*, 614.
[32] L. Zhou, Y. Peng, N. Zhang, R. Du, R. Hübner, X. Wen, D. Li, Y. Hu, A. Eychmüller, *Adv. Opt. Mater.* **2021**, *9*, 2100352.
[33] V. Zielasek, B. Jürgens, C. Schulz, J. Biener, M. M. Biener, A. V. Hamza, M. Bäumer, *Angew. Chem., Int. Ed.* **2006**, *45*, 8241.